Climate Dynamics (2003) 20: 401–413
DOI 10.1007/s00382-002-0282-4

B. Chen · W.C. Chao · X. Liu

Enhanced climatic warming in the Tibetan Plateau due to doubling CO2: a model study

Received: 5 April 2002 / Accepted: 7 August 2002 / Published online: 19 December 2002

Abstract The National Center for Atmospheric Research (NCAR) regional climate model (RegCM2), together with initial conditions and time-dependent lateral boundary conditions provided by a 130-year transient increasing CO_2 simulation of the NCAR Climate System Model (CSM), has been used to investigate the mechanism of ground warming over the Tibetan Plateau (TP). The model results show that when CO_2 in the atmosphere is doubled, a strong ground warming occurs in the TP. Two regions within it with the largest warming are in the eastern TP (region I) and along the southwestern and western slopes (region II). Moreover, in region I the ground warming in the winter half year is stronger than that in the summer half year, but in region II the warming difference between the seasons becomes opposite to that in region I, i.e., the warming is strong in the summer half year and weak in the winter half year. There are indications that the summer monsoon enhances but the winter monsoon weakens when CO_2 is doubled. A strong elevation dependency of ground warming is found in region I for the winter half year, and in region II for both winter and summer half years at elevations below 5 km. The simulated characteristics of ground warming in the TP are consistent with the observations. In region I, when CO_2 is doubled, the cloud amount increases at lower elevations and decreases at higher elevation for the winter half year. As a consequence, at lower elevations the short wave solar radiation absorbed at the surface declines, and the downward long wave flux reaching the surface enhances; on the other hand, at higher elevations the surface solar radiation flux increases and the surface infrared radiation flux shows a more uniform increase. The net effect of the changes in both radiation fluxes is an enhanced surface warming at higher elevations, which is the primary cause of the elevation dependency in the surface warming. In the summer half year the cloud amount reduces as a result of doubling CO_2 in region I for all elevations, and there is no elevation dependency detected in the ground warming. Furthermore, there is little snow existing in region I for both summer and winter half years, and the impact of snow-albedo feedback is not significant. In region II, although the changes in the cloud amount bear a resemblance to those in region I, the most significant factor affecting the surface energy budget is the depletion of the snow cover at higher elevations, which leads to a reduction of the surface albedo. This reduction in turn leads to an enhancement in the solar radiation absorbed in the surface. The snow-albedo feedback mechanism is the most essential cause of the elevation dependency in the surface warming for region II.

B. Chen
GEST Center, University of Maryland,
Baltimore County,
Baltimore, MD, USA

W.C. Chao
NASA/Goddard Space Fight Center,
Greenbelt, MD, USA

X. Liu
Institute of Earth Environment,
Chinese Academy of Sciences, Xian, China

B. Chen (✉)
GSFC/NASA, Mail Code 913,
Greenbelt, MD 20711, USA
E-mail: bdchen@climate.gsfc.nasa.gov

1 Introduction

There are growing concerns over the climate change in high elevation areas. Specifically, the climatic warming induced by the greenhouse gases could severely impact human activities and ecosystems in these regions. A number of studies have presented evidence that surface climate change associated with the global warming at high elevation sites shows more pronounced warming than that at low elevation sites, i.e., an elevation dependency of climatic warming. Beniston et al. (1997)

indicated that, as far as the same latitudes of northern land are concerned, the observed surface air temperature change seems to be related to elevation. In addition, Beniston and Rebetez (1996) found that the surface climate change in the Swiss Alps in association with the global warming displayed an altitudinal dependency. In the Tien Shan of central Asia, during the second half of the twentieth century, the warming trend in the regions over 2 km above sea level (a.s.l.) appeared to be greater than that below 2 km a.s.l. (e.g., Aizen et al. 1997). Using an early version of the National Center of Atmosphere Research (NCAR) regional climate model, Giorgi et al. (1997) showed that the snow-albedo feedback may be responsible for the excessive warming in the Swiss Alps. From an ensemble of climate change experiments with increasing greenhouse gases and aerosols using an air–sea coupled climate model, Fyfe and Flato (1999) found a marked elevation dependency of the simulated surface screen temperature increase over the Rocky Mountains.

The Tibetan Plateau (TP) is located in central Asia with a mean elevation of more than 4 km a.s.l. and an area of about 2.3×10^6 km^2. It is surrounded by the highest mountains in the world, such as the Himalayas, Pamir, Kunlun Shan and others, and exerts profound thermal and dynamical influences on the local weather and climate as well as on the atmospheric circulation in the Northern Hemisphere (e.g., Manabe and Terpstra 1974; Yeh and Gao 1979; Manabe and Broccoli 1990; Yanai et al. 1992; Kutzbach et al. 1993). Analysis of ice core from the TP indicates that there was a significant increase in the ground temperature over the last few decades (e.g., Thompson et al. 1993; Yao et al. 1995), which appeared to be associated with the retreat of most mountain glaciers on the TP (see Tang et al. 1998 for details). Using almost all the available instrumental records, Liu and Chen (2000) showed that the main portion of the TP had experienced significant surface warming since the mid-1950s, especially in winter. The linear rates of increase in the surface air temperature in the TP during the period of 1955–1996 were about 0.16 °C/decade for the annual mean and 0.32 °C/decade for the winter mean, which exceeded those for the same latitudinal zone in the Northern Hemisphere during the same period. The surface warming in different parts of the TP was not completely the same in form, and the stronger warming trend occurred in the central, eastern and northwestern TP. In addition, they found that there was a tendency for the warming trend to increase with elevation in the TP as well as its surrounding areas.

The cause of the recent surface warming in the TP has not been fully understood. However, numerical experiments have shown that, with enhanced greenhouse gases, there is an increase in the TP surface air temperature for most current climate models (Manabe et al. 1991; Cubasch et al. 1992; Murphy and Mitchell 1995; Houghton et al. 1996). This fact implies that the observed TP warming could be attributed to increased greenhouse gases in the atmosphere, which are believed to result from human activities. Moreover, Liu and Chen (2000) have made a detailed analysis of the TP surface air temperature from the doubling CO_2 experiments produced by three well-known global climate models. The results indicate that, although the surface warming in the TP is evident, the elevation dependency of the warming as shown in the observations could not be found. They argued that this disagreement may be owing partly to the coarse resolution of the models and partly to the inadequate treatment of physical processes, in particular, land surface processes in complex topographic areas like the TP.

With its vast area the TP has unique topography, landscape and climate compared with other high elevation regions. It is natural to consider that the climate warming induced by enhanced greenhouse gases and its elevation dependency in the TP are closely associated with the TP's inherent complexity of topography and climatic variability among various terrestrial regimes. Therefore, in order to investigate the climatic warming over the TP, the use of high-resolution models is essential. In this study, by using a high-resolution regional climate model, the climatic response in the TP to a doubling of CO_2 in the global atmosphere will be examined and the focus will be on the ground warming and its mechanism.

In the next section the model used and experimental design will be outlined. A brief description of the lateral boundary conditions will also be given in this section. Section 3 will show the results simulated from two three-year integrations. Section 4 will discuss the surface energy budget and the relevant atmospheric and surface processes that make impacts on the surface energy exchange. Conclusion and discussion will be presented in Section 5.

2 Description of model used and experimental design

The latest version of the NCAR regional climate model version 2 (RegCM2) is used. The dynamical component of the RegCM2 is essentially the same as that of the MM4 (The NCAR-Pennsylvania State University Meso-scale Model version 4), which is a compressible, grid point model with hydrostatic balance and vertical σ-coordinates. Exceptions are the use of a split-explicit time integration scheme and of an algorithm for reducing horizontal diffusion in the presence of steep topographical gradients (Giorgi et al. 1993a, b). A number of physics parametrization schemes have been adopted in the model for applications to climate studies. The radiative transfer package is that of the NCAR Community Climate Model version 3 (CCM3), and the boundary layer scheme from Holtslag et al. (1990). The latest version of BATS 1E (Biosphere–Atmosphere Transfer Scheme) (Dickinson et al. 1992) was incorporated into the model to perform the surface physics calculations. The mass flux scheme of Grell et al. (1994) was implemented for cumulus convection parametrization.

Figure 1 illustrates the domain and topography in our study. The domain is covered by dotted lines, which represent the longitudes and latitudes included in the model's domain, and contains most of Asia and a portion of Eastern Europe. It should be pointed out that the model grid points are projected on a Lambert conformal projection map, and that to display all model points on a conventional longitude/latitude grid map, certain extraneous

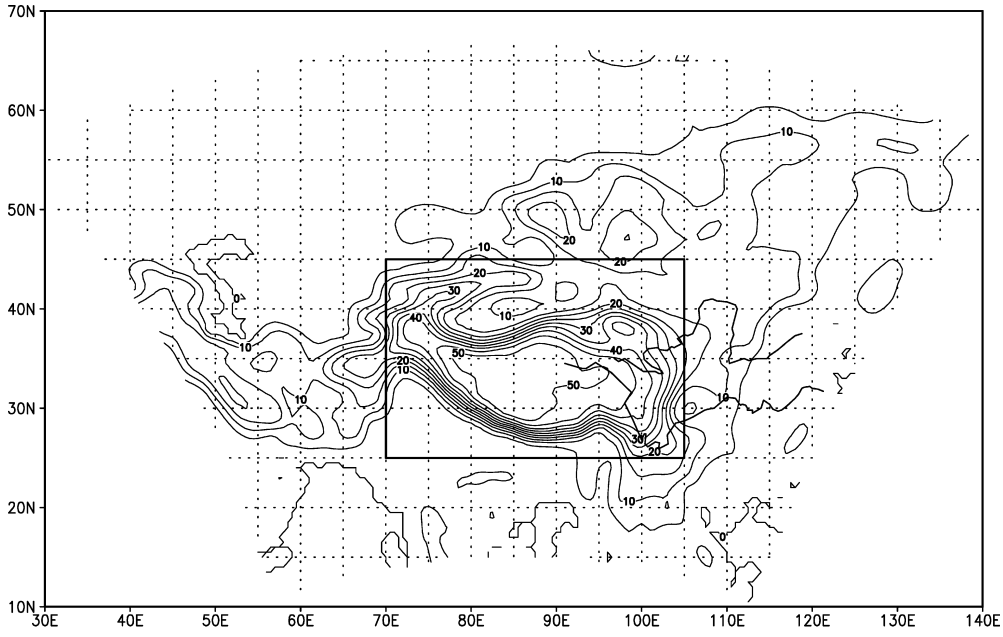

Fig. 1 Model domain and topography (units are 100 m). Also shown is the area selected for analysis

longitude/latitude points which do not belong to the model's domain have to be included in the plot. Also shown in Fig. 1 is a sub-region that encompasses the entire TP and is selected to demonstrate our results. Because the selected sub-region is far from the lateral boundary of the model, the simulation to be shown in the subsequent sections is believed to be mostly the results of the model internal physical processes and relevant local forcing. A 60 km grid size and 14 levels with the model top at 80 hPa are used. The climate in the model's domain, where the land surface type varies from tropical rain forest to desert, is characterized by remarkable monsoon circulations, and the spatial pattern of the precipitation is frequently enhanced by topographical forcing. To evaluate the model's performance in the domain, the RegCM2 was first integrated for a 4-month period (June–September, 1994) using the TOGA analyses of European Centre for Medium-Range Weather Forecasts (ECMWF) as the lateral boundary conditions. The results (not shown) indicate that the RegCM2 did fairly well in the simulations of precipitation, ground temperature and monsoon circulations. Moreover, Kato et al. (2001) evaluated the performance of RegCM2 for the simulation of climate change in East Asia caused by global warming, and indicated that the typical precipitation phenomena during the winter and summer monsoons were well reproduced in the RegCM2.

The lateral boundary conditions used for our experiments are from a 130-year transient increasing CO_2 run produced by the NCAR Climate System Model (CSM), in which atmospheric CO_2 was increased at a rate of 1% y^{-1}. The models included in the NCAR CSM are the NCAR Community Climate Model (CCM) (atmosphere model version CCM3.2), the NCAR Land Surface Model (version 1), the NCAR Sea Ice Model (version CSIM-3.5.3), and the NCAR global Ocean Model (version NCOM-1.1). The various component models are connected by a flux coupler in which interfacial fluxes between the models are calculated and are distributed to all component models while ensuring the conservation of fluxed quantities. Meehl et al. (2000) indicated that the simulated globally averaged surface air temperature increase near the time of CO_2 doubling is about 1.43 °C, with an increase of globally averaged precipitation of 2%. In addition, the greatest surface warming is found in the winter hemisphere at high latitudes, particularly in the Northern Hemisphere during December–February (DJF). As compared with other global coupled models, global warming due to increased CO_2 is relatively low in the NCAR CSM (Kattenberg et al. 1996).

Figure 2 shows the 12-month running means of monthly averaged surface air temperatures for the globe (thin solid line) and for the area selected in our analysis (thick solid line). In Fig. 2, the years when CO_2 level was held at the present day value (355 ppm) and the years when doubling CO_2 was achieved are highlighted. Over the analysis area the surface air temperature near the time of CO_2 doubling increases about 1.9 °C. Mean amplitude of inter-annual fluctuation (~0.4 °C) is larger than that in the global mean, however, and is far smaller than the warming induced by doubling CO_2. In our study the CSM model results starting from years 10 and 80 are selected as the initial conditions and boundary conditions for the control and $2\times CO_2$ runs respectively. The lateral and surface boundary conditions are supplied at 6-h intervals from the run of the NCAR-CSM with a horizontal resolution of T42. Both runs have been integrated for three years and four months, and the first four months are neglected in the analysis to ensure that the climatology obtained is in dynamical equilibrium between the lateral boundary forcing and the internal model physics and dynamics. Moreover, to be consistent with the boundary conditions, the CO_2 concentration used in the radiation transfer package was set to 355 ppm in the control run and 710 ppm in the $2\times CO_2$ run. Details of the parametrization for the CO_2 absorber are given in Kiehl and Briegleb (1991). For both simplicity and an attempt to include as much information as possible, the outputs are only averaged into the winter half year (October to March) and the summer half year (April to September). Compared with conventional means (e.g., JJA as summer and DJF as winter etc.), such a choice of analysis period is rather representative.

3 The enhanced climatic warming signal detected from the experiments

Figure 3a–c shows the ground temperature simulated from the control run (Fig. 3a) and the $2\times CO_2$ run (Fig. 3b), and the difference between them (Fig. 3c) for the winter half year. The ground temperature patterns (Fig. 3a, b) closely follow the topographic characteristics of the TP with cooler temperature at higher altitudes and strong temperature gradient corresponding to large elevation gradient. In comparison with the simulation from the CSM (not shown), the ground temperature produced by the RegCM2 shows a more

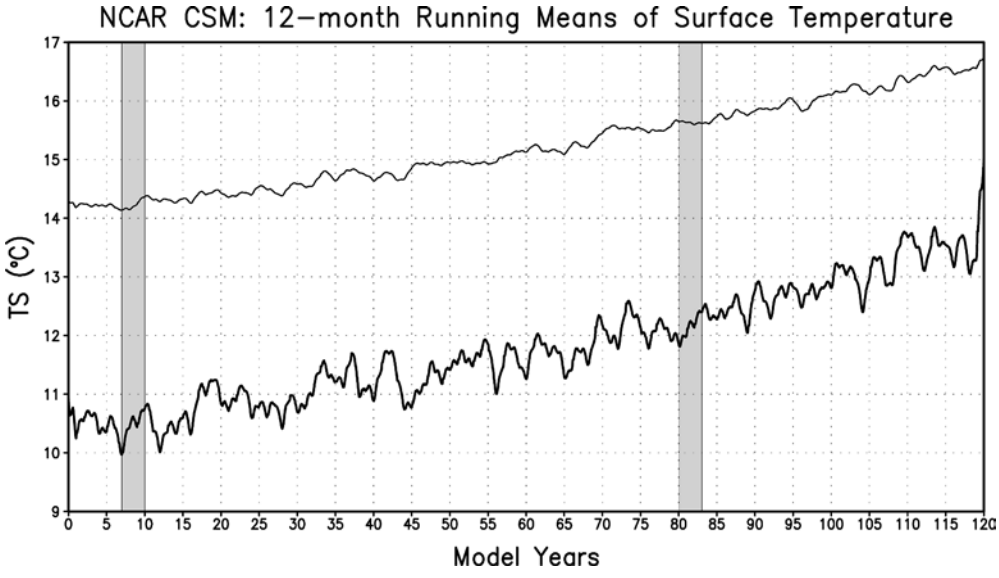

Fig. 2 NCAR CSM simulated 12-month running means of monthly averaged surface air temperatures for the globe (*thin solid line*) and for the area selected in the analysis (*thick solid line*) as a function of model years. *Shaded* are the years when CO_2 level was held at the present day value (355 ppm) and the years when doubling CO_2 was achieved

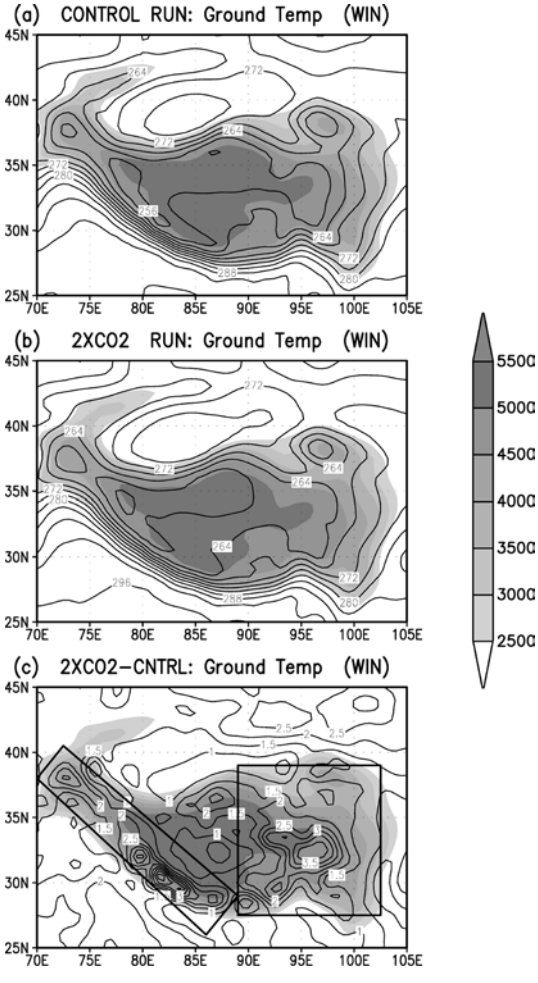

Fig. 3a–c Simulated ground temperature for **a** the control run, **b** the 2×CO_2 run and **c** the difference between them for the winter half year (units: °K). *Shaded* is topography

detailed structure. In Fig. 3c, it can be seen that in the winter the ground temperature warming covers almost the entire TP, and two regions with maximum ground temperature increases can be observed in the eastern TP and along the southwestern and western slopes. Therefore these two regions with the strongest warming are selected, and labeled as region I and II, for detailed analysis. In particular, region II covers the highest mountains, such as the Himalayas etc. Figure 4a–c is the same as Fig. 3a–c but for the summer half year. In the summer half year, the surface warming is reduced and more evenly distributed in region I and, however, substantially enhanced in region II. It is found that in region I the ground warming in the winter half year is stronger than that in the summer half year, and that in region II the warming difference between the seasons becomes opposite to that in region I, i.e., the warming is strong in the summer half year and weak in the winter half year. This strong seasonality in the ground warming is considered to be associated with the remarkable monsoon circulation around the TP and the surface characteristics as well, and will be demonstrated shortly. In addition, another small region with large increase in the ground temperature is found in the middle of northern slope in Fig. 4c, but it will not be studied because of its much smaller area in comparison with region I and II. Furthermore the statistical significance of the ground temperature difference between two runs is tested (see Appendix A), and the result indicates that the area–averaged ground temperature difference between two runs is statistically significant and conclusive at the 95% significance level even though our RegCM runs are relatively short.

In order to provide a planetary scale background for the ground temperature changes shown in Figs. 3a–c and 4a–c, as well as to obtain clues on the changes in the monsoon circulations resulting from the doubling of

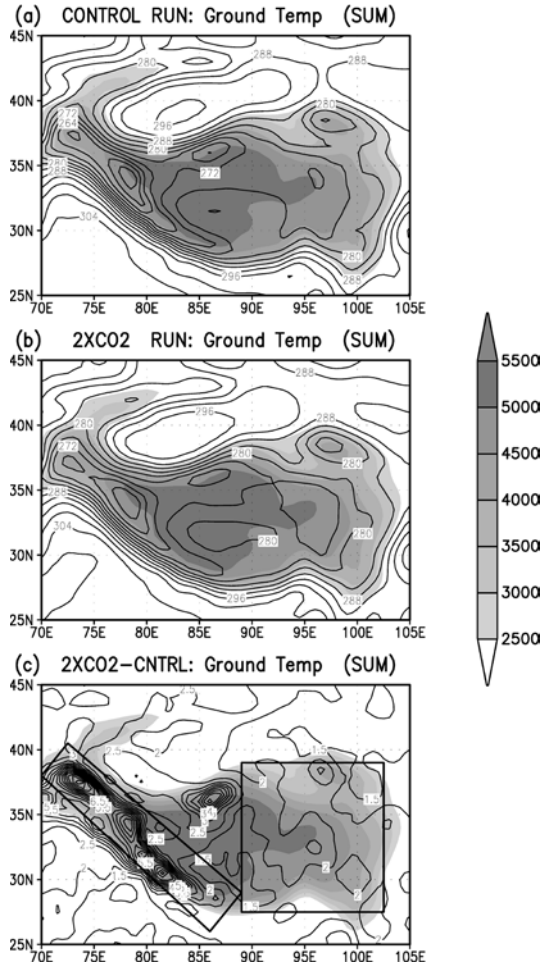

Fig. 4a–c The same as Fig. 3, but for the summer half year

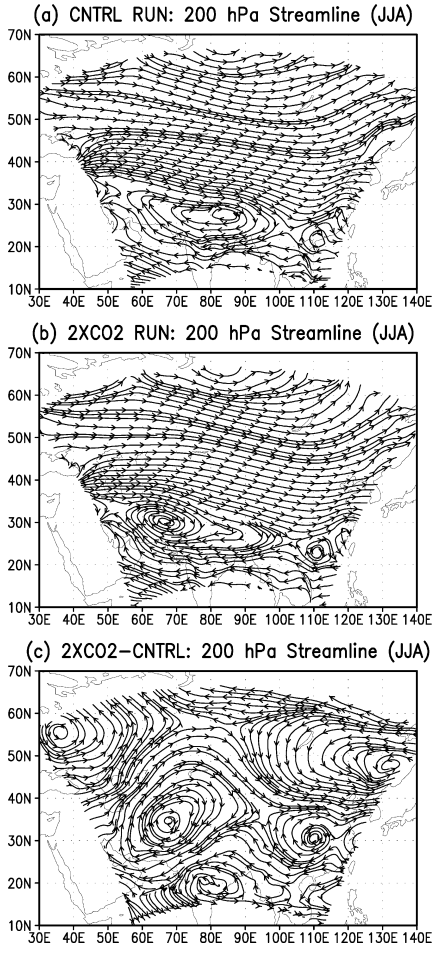

Fig. 5a–c JJA mean 200 hPa stream lines for **a** the control run, **b** the $2\times CO_2$ run and **c** the difference

CO_2, June–August (JJA) and December–February (DJF) mean 200 hPa stream lines from the control run, $2\times CO_2$ run and the difference between them are illustrated for the whole model domain in Figs. 5a–c and 6a–c. The most striking features associated with summer monsoon in Fig. 5a (control run) are the huge anti-cyclonic circulation (the Tibetan High) over southern Asia centered at the TP and the associated easterly jet to the south of the TP. Compared with observation (not shown), the simulated center of the Tibetan High shifts westward about 4° longitudes. In addition, strong westerlies are dominant in the middle and high latitudes and a deep trough is seen close to the eastern coast of Asia. In the $2\times CO_2$ run the Tibetan High is intensified with enhanced wind speed and its center moves north-eastward to central Asia (Fig. 5b). In Fig. 5c a strong intensification of anti-cyclonic circulation is found along a wide latitude band centered at 30°N with two maxima over central Asia and China. In addition, enhanced cyclonic circulations are seen over the high latitudes and the sub-tropical regions, however the enhancement in the high latitudes is much stronger. This change in the circulation is closely related to warmer air mass over the regions from central Asia to the TP (not shown), which results in the intensified temperature gradients in both the north–south and east–west directions. In DJF mean, westerly is dominating over the whole model's region for both the control and $2\times CO_2$ runs (Fig. 6a, b). As shown in Fig. 6c, the westerly is enhanced in South Asia for the $2\times CO_2$ run, and the intensified southerly is over Mongolia and flanked by an enhanced cyclone to the west and an anti-cyclone to the east. Based on Webster and Yang's broad monsoon index (Webster and Yang 1992), which is the magnitude of the vertical shear zonal wind averaged in the region (0°–20°N; 40°E–110°E) and has a clear relationship with the strength of the heating over South Asia, in JJA the enhanced easterlies at upper level over South Asia, together with the enhanced westerlies at lower level (not shown) give an indication of a stronger summer monsoon in the $2\times CO_2$ run, although a small portion of the region defined by Webster and Yang (1992) is included in the model's domain. On the other hand, in DJF the winter monsoon seems to become weaker in terms of the sea level pressure (not shown), for example, the strength of the Mongolia high tends to decline in the $2\times CO_2$ run. However it should be pointed out that our model's domain is too small to cover the whole monsoon regions, thus further

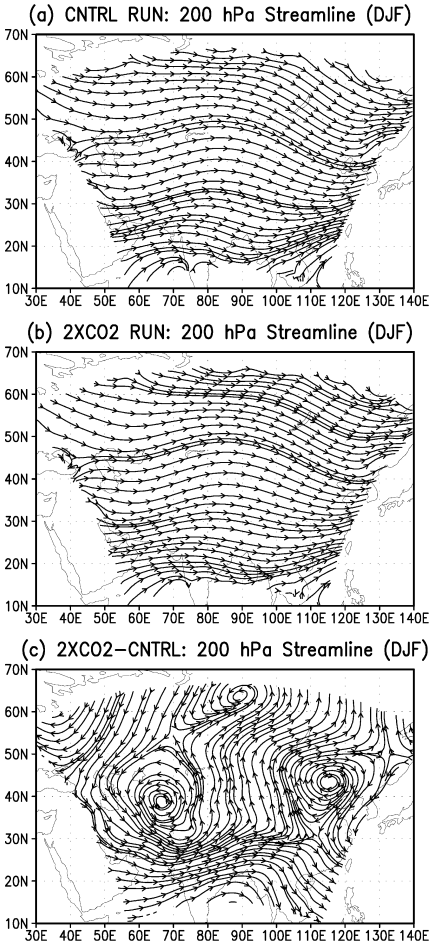

Fig. 6a–c The same as Fig. 5, but for DJF mean

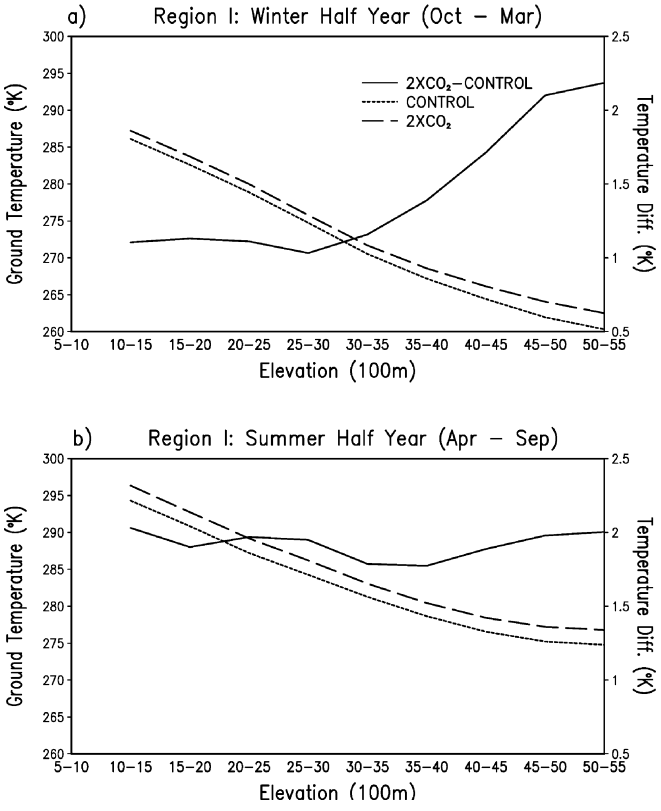

Fig. 7a, b The ground temperature from the $2\times CO_2$ run, the control run and the difference between them as functions of elevation in region I for **a** the winter and **b** the summer half years

clarification needs to be made by analyzing simulations with a larger domain.

The ground temperature differences between the $2\times CO_2$ and control runs in region I are plotted in Fig. 7a, b as functions of elevation over the model grid points for the summer and winter half years respectively. In Fig. 7a, b, topographical elevation is divided into 10 categories with a 500-m interval, i.e., 0.5–1.0 km, 1.0–1.5 km,…,5.0–5.5 km, and the value of temperature difference is obtained by averaging results over all grid points in each elevation category. It is noticed that there is no grid point fitting in the category of 0.5–1.0 km. In the winter half year (Fig. 7a) the ground warming is about 1.0 to 1.1°K at the elevations below 3.0 km and shows a rather uniform distribution with elevation. The most remarkable feature is a tendency of ground temperature warming increasing with elevation above 3.0 km, and the maximum temperature increase is 2.2°K at the elevations of 4.5 to 5.5 km. This elevation dependency of surface warming in the winter half year is consistent with Liu and Chen's observational study (2000). For the summer half year (Fig. 7b), the surface warming is approximately equal among the elevation categories, and the ground temperature has increased by 2°K with a deviation about ± 0.1°K. There is no elevation dependency of surface warming, also in agreement with Liu and Chen (2000). Considering that the most meteorological stations used in Liu and Chen (2000) are located in the eastern TP, our simulated surface warming is quite successful in terms of being consistent with the observations.

Figure 8a, b is the same as Fig. 7a, b but for region II. In the winter half year the strongest warming is about 2.5°K at the elevations of 4.5–5.0 km and the weakest warming 0.5°K below 2.5 km (Fig. 8a). An elevation dependency of surface warming is evident although the warming at the highest elevations (5.0–5.5 km) is slightly weaker than that at the elevations of 4.5–5.0 km. In the summer half year (Fig. 8b), the most outstanding feature is that the surface warming is substantially enhanced with a maximum of 5.2°K at the elevations of 4.0–4.5 km, and a minimum of 1.4°K around 2.0–2.5 km. At the elevations between 2.0 km and 4.5 km, the surface warming intensifies from 1.5°K to 5.2°K with elevation increasing and further declines to 3.8°K at the elevations of 5.0–5.5 km. It should be pointed out that because there are few meteorological stations and no continuous records were collected in region II, it is difficult to verify our simulations with observations in that region.

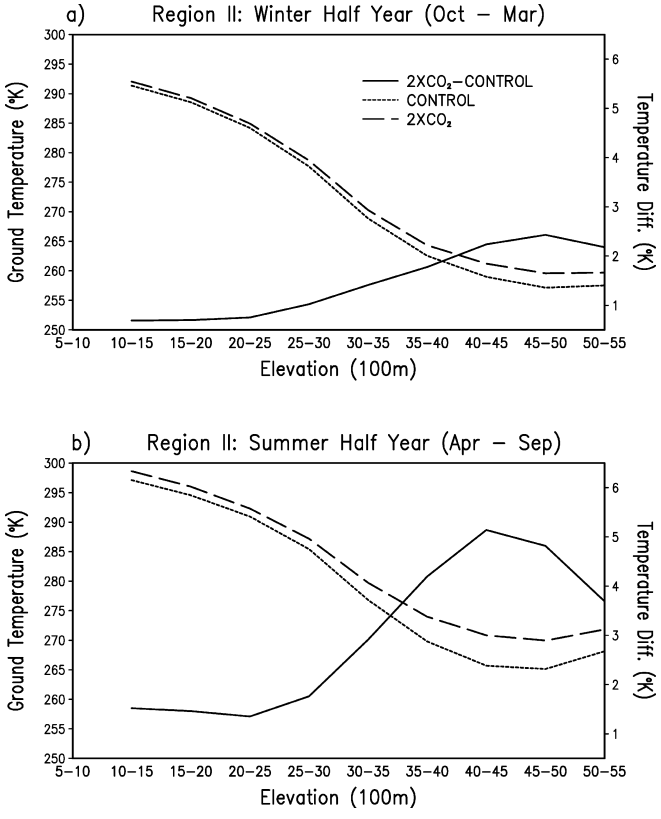

Fig. 8a, b The same as Fig. 7, but for region II

4 The physical processes responsible for the surface warming in the TP

4.1 Region I

4.1.1 Surface energy budget

The ground temperature is determined by surface energy exchanges and governed by the surface energy budget equation, which can be written as

$$C\frac{\partial T_g}{\partial t} = S_g + F_{IR}^{\downarrow} - F_{IR}^{\uparrow} - SHF - LHF - S_m$$

where C is the total heat capacity of ground, T_g is ground temperature, S_g is surface absorbed solar flux, $F_{IR}^{\downarrow}$ is downward long-wave flux reaching surface, $F_{IR}^{\uparrow}$ is infrared radiation flux emitted from ground, SHF and LHF represent atmospheric sensible and latent heat fluxes from ground to atmosphere respectively, and S_m is the energy flux associated with snow melt in the presence of snow. In order to demonstrate the roles of various surface energy exchanges in the local ground temperature response, an analysis of the surface energy balance in region I and region II (see Sect. 4.2) has been made.

Figure 9a and c shows the differences between the $2\times CO_2$ and control run for S_g, $F_{IR}^{\downarrow}$, $F_{IR}^{\uparrow}$, SHF and LHF, which are displayed as functions of elevation in region I for the winter and summer half years. In addition, the differences in combinations of ($S_g + F_{IR}^{\downarrow}$), ($SHF + LHF$) and ($S_g + F_{IR}^{\downarrow}$) – ($SHF + LHF$) are also plotted in Fig. 9b and d for the purpose of interpreting the results more easily. Hereafter the difference

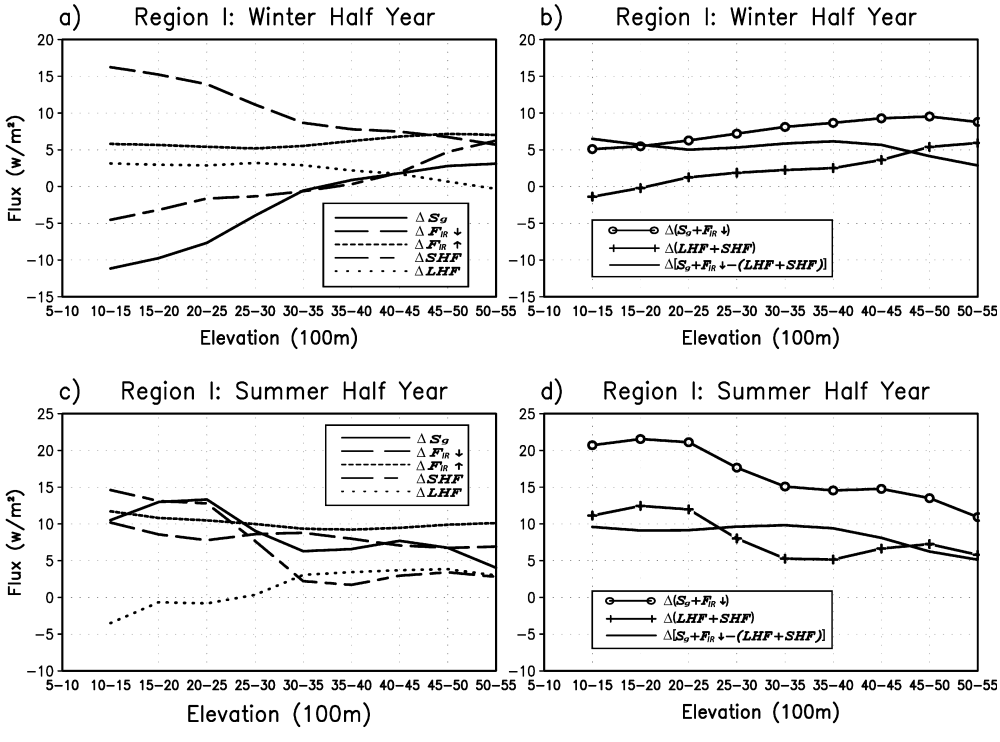

Fig. 9a–d The surface flux differences between $2\times CO_2$ and control run as functions of elevation in region I. Shown are differences in **a** the surface absorbed solar flux (ΔS_g), the downward long-wave flux at the surface ($\Delta F_{IR}^{\downarrow}$), the infrared radiation flux emitted from the surface ($\Delta F_{IR}^{\uparrow}$), the surface sensible heating flux (ΔSHF) and latent heating flux (ΔLHF), and **b** the combinations of $\Delta(S_g + F_{IR}^{\downarrow})$, $\Delta(SHF + LHF)$ and $\Delta[(S_g + F_{IR}^{\downarrow}) - (SHF + LHF)]$ for the winter as well as **c, d** for the summer half years

between two runs is denoted by Δ, for instance, ΔS_g represents difference in S_g (that of the $2\times CO_2$ run minus that of the control run) and so forth.

During the winter half year (Fig. 9a), below the elevations of 3.0–3.5 km ΔS_g is negative and its magnitude declines as elevation increasing, however $\Delta F_{IR}^{\downarrow}$ is positive but its magnitude decreases as well showing a characteristic compensating mechanism. At the elevations above 3.0–3.5 km both ΔS_g and $\Delta F_{IR}^{\downarrow}$ are positive, and their magnitudes show a slight increase in ΔS_g and a decrease in $\Delta F_{IR}^{\downarrow}$ as elevation increases. The characteristics of ΔS_g and $\Delta F_{IR}^{\downarrow}$ are closely associated with the changes in cloud effects related to the doubling of CO_2, and the details will be presented shortly. From Fig. 9b it can be seen that $\Delta(S_g + F_{IR}^{\downarrow}) > 0$ is shown at all elevations, i.e., $(S_g + F_{IR}^{\downarrow})$ in the $2\times CO_2$ run is enhanced, and the magnitude becomes enlarged with increasing elevation indicating a strong elevation dependency. $(S_g + F_{IR}^{\downarrow})$ acts to warm the surface, therefore the enhanced $(S_g + F_{IR}^{\downarrow})$ in the $2\times CO_2$ run is most responsible for the surface warming in the TP and its elevation dependency as well. Below the elevations of 3.0–3.5 km, ΔSHF is negative and its magnitude declines with elevation. Above 3.5–4.0 km ΔSHF turns positive and the magnitude shows a steady increase with elevation. At all elevations ΔLHF is positive and relatively uniform. Except at the elevations below 3.5 km where negative ΔSHF exits, both ΔSHF and ΔLHF act to cool the surface. Also shown in Fig. 9b, $\Delta(SHF + LHF)$ offsets some of $\Delta(S_g + F_{IR}^{\downarrow})$. Finally, as a result of the greater ground temperature, the surface emission of infrared radiation ($F_{IR}^{\uparrow}$) enhances at all elevations to make the surface energy budget balance.

For the summer half year (Fig. 9c), at all elevations both ΔS_g and $\Delta F_{IR}^{\downarrow}$ are positive indicating enhanced S_g and $F_{IR}^{\downarrow}$ in the $2\times CO_2$ run. Moreover the magnitudes of ΔS_g and $\Delta F_{IR}^{\downarrow}$ show a feature of "out-phase" with respect to elevation in the sense that an enhancement in one flux is corresponding to a reduction in the other flux and *vice versa*. As shown in Fig. 9d, since the larger magnitude is at lower elevations and the smaller one at higher elevations, there is a reverse elevation dependency shown in $\Delta(S_g + F_{IR}^{\downarrow})$. Although $\Delta(S_g + F_{IR}^{\downarrow}) > 0$ is a primary cause of ground warming in the $2\times CO_2$ run, unlike the winter half year, it does not show a controlling influence on the elevation dependency of ground warming. In Fig. 9c $\Delta SHF > 0$ exists at all elevations and the largest magnitude is below 3.0–3.5 km elevations. In addition, $\Delta LHF < 0$ is shown at the elevations below 3.0 km and it turns into positive values above. As seen in Fig. 9d, the net effect of $\Delta(SHF + LHF)$ acts to cool the surface because of its positive value, and offsets a portion of the enhanced $(S_g + F_{IR}^{\downarrow})$. It is that the combination of $\Delta(S_g + F_{IR}^{\downarrow}) - \Delta(SHF + LHF)$ determines the distribution of surface warming with elevation, which is balanced by the enhanced $F_{IR}^{\uparrow}$ resulting from warmer ground temperature.

4.1.2 Factors responsible for the change in the surface energy exchange

From an energetic point of view, to make the surface energy budget balance, changes in the surface radiative heat fluxes, which are due to enhanced greenhouse effects resulting from a doubling of CO_2, must be compensated by changes in other surface energy fluxes. This energy balance is achieved, from a dynamical point of view, by adjusting the atmosphere to a new structure to be compatible with the new energetic constraints through the dynamics and thermodynamics operating within the atmosphere. Among various surface energy fluxes, the enhanced $(S_g + F_{IR}^{\downarrow})$ is the primary cause of surface warming in the TP, and is determined by many factors including the surface states, such as surface albedo which most depends on the particular feature of the surface, e.g., the presence of snow and vegetation etc., the temperature distribution and trace gases throughout the atmosphere, and especially the distribution and nature of cloudiness. Moreover, $F_{IR}^{\uparrow}$, SHF and LHF act to counter the enhanced $(S_g + F_{IR}^{\downarrow})$. Amongst them $F_{IR}^{\uparrow}$ depends only on the state of the surface, and SHF and LHF depend both on the surface and on the atmospheric structure near the surface.

In region I there is little snow for both winter and summer half years, and the impact of snow-albedo feedback on ΔS_g is not significant. The cloud effects related to the doubling of CO_2 are essential to the characteristics of $\Delta(S_g + F_{IR}^{\downarrow})$. Figure 10a, b illustrates the cloud amount (cloud fraction) difference between the $2\times CO_2$ and control run in region I for the cool (Fig. 10a) and warm (Fig. 10b) seasons, in which the differences are plotted as functions of both elevation and height (pressure). In the winter half year (Fig. 10a) a significant increase in the cloud amount for the $2\times CO_2$ run can be found in the elevations below 3.0 km under 400 hPa, and a decrease above 3.5 km. The enhanced cloud amount, in particular, in middle and low levels, exerts two compensating effects on the radiation field. On one hand, increased cloudiness in lower elevations reflects a significant portion of the incoming solar flux, which leads to a decrease in S_g; on the other hand, it traps more outgoing thermal infrared fluxes emitted from the atmosphere below the clouds and from the surface, which results in an increase in $F_{IR}^{\downarrow}$. At elevations above 3.5 km, the cloud amount is reduced and the reduction leads to an increase in S_g. Because of smaller cloud amount, $F_{IR}^{\downarrow}$ shows a relatively uniform increase at elevations above 3.5 km, which is mainly due to doubling CO_2. Figure 11a, b shows the precipitation of region I for the control and $2\times CO_2$ runs together with their difference in the winter and summer half years respectively, in which the precipitation and differences are plotted as functions of elevation. In the winter half year (Fig. 11a), in association with the enhanced cloud amount at lower elevations, the precipitation increases at the same locations with a maximum around 2.0–2.5 km, and with elevation becoming higher, the

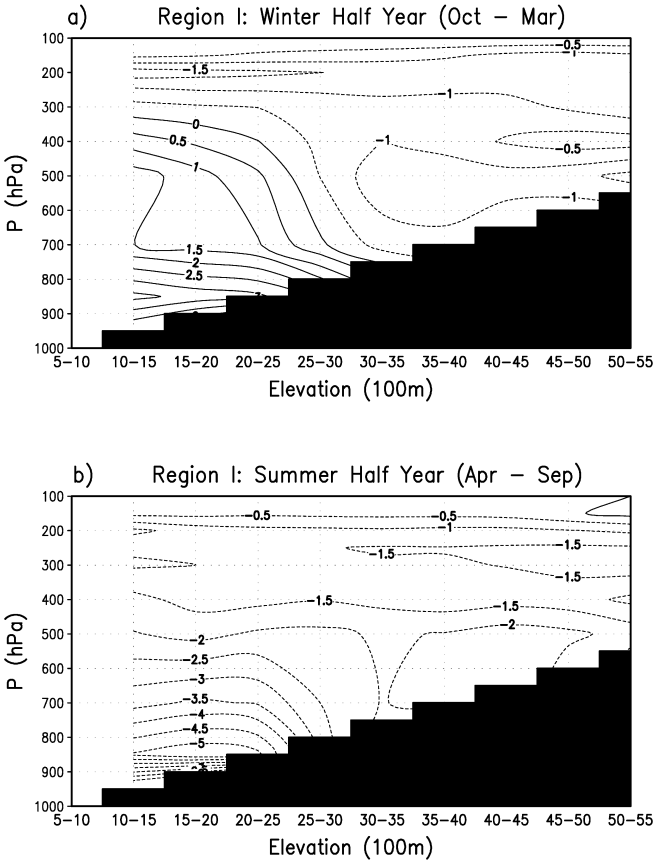

Fig. 10a, b The difference of cloud amount (cloud fraction) between $2\times CO_2$ and control run as a function of elevation and pressure in region I for **a** the winter and **b** the summer years (units: %)

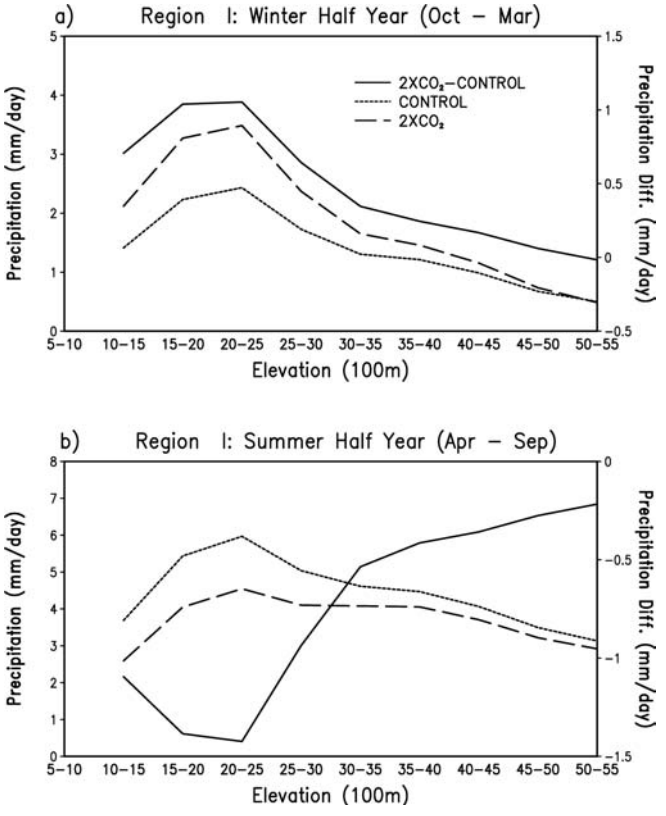

Fig. 11a, b The precipitation from the $2\times CO_2$ run, the control run and the difference between them as functions of elevation in region I for **a** the winter and **b** the summer half years

precipitation increases tend to be weaker. Along with the enhanced precipitation *LHF* increases but *SHF* decreases, and the net effect of $\Delta(SHF + LHF)$ is to act to cool the surface as shown in Fig. 9a, b. In addition, there is only small snow cover found at higher elevations in region I, and therefore the effects of the snow cover differences between two runs can be neglected compared with those in region II (see Fig. 12a, b). In the summer half year (Fig. 10b), the cloud amount reduces at all elevations with more reduction at lower elevations. Because of reduced cloud amount, S_g enhances at all elevations with a stronger enhancement at lower locations, and the increase in $F_{IR}^{\downarrow}$ shows a rather uniform distribution with elevation. Associated with the decreases in cloud amount, precipitation (Fig. 11b) declines at all elevations and the largest declines occur at lower locations. As a result of the reduced precipitation, *LHF* decreases but *SHF* increases, $\Delta(SHF + LHF)$ is positive and acts to cool the surface.

4.2 Region II

4.2.1 Surface energy budget

Figure 12a, d is the same as Fig. 9a, d but for region II. In the winter half year (Fig. 12a), ΔS_g is negative in the elevation range of 1.0 km to 3.0 km and the magnitude becomes smaller as elevation increases. As the topography reaches up to more than 3.0 km ΔS_g turns positive and its maximum magnitude can be found around the elevations of 4.0–5.0 km indicating an enhancement in solar radiation absorbed at the surface for the $2\times CO_2$ run. On the other hand, positive $\Delta F_{IR}^{\downarrow}$ exists at all elevations, and a maximum shows at lower elevations and a minimum at higher elevations. Although ΔS_g and $\Delta F_{IR}^{\downarrow}$ exhibit a compensating characteristic similar to that in region I (see Fig. 9a), unlike in region I, the net solar radiation absorbed at the surface $\Delta(S_g + F_{IR}^{\downarrow})$ does not display any tendency of an elevation dependency (see Fig. 12b). Moreover ΔLHF is positive at all elevations indicating enhanced *LHF* in the $2\times CO_2$ run, and a significant increase in *LHF* can be found below 3.0–3.5 km (up to 10 w/m^2) compared with that in the higher elevations. However, below 3.0–3.5 km ΔSHF is negative and *SHF* exhibits a maximum decrease in the $2\times CO_2$ run at the elevations where the largest increase in *LHF* shows, although a slight increase at the lowest location. The combined effect of ΔLHF and ΔSHF (Fig. 12b) counteracts the enhanced $(S_g + F_{IR}^{\downarrow})$ by acting to cool the surface at all elevations. In consequence, the combination of $\Delta(S_g + F_{IR}^{\downarrow}) - \Delta(LHF + SHF)$ exhibits a relatively weak elevation dependency, and is balanced by the enhanced surface emission of infrared radiation $(F_{IR}^{\uparrow})$.

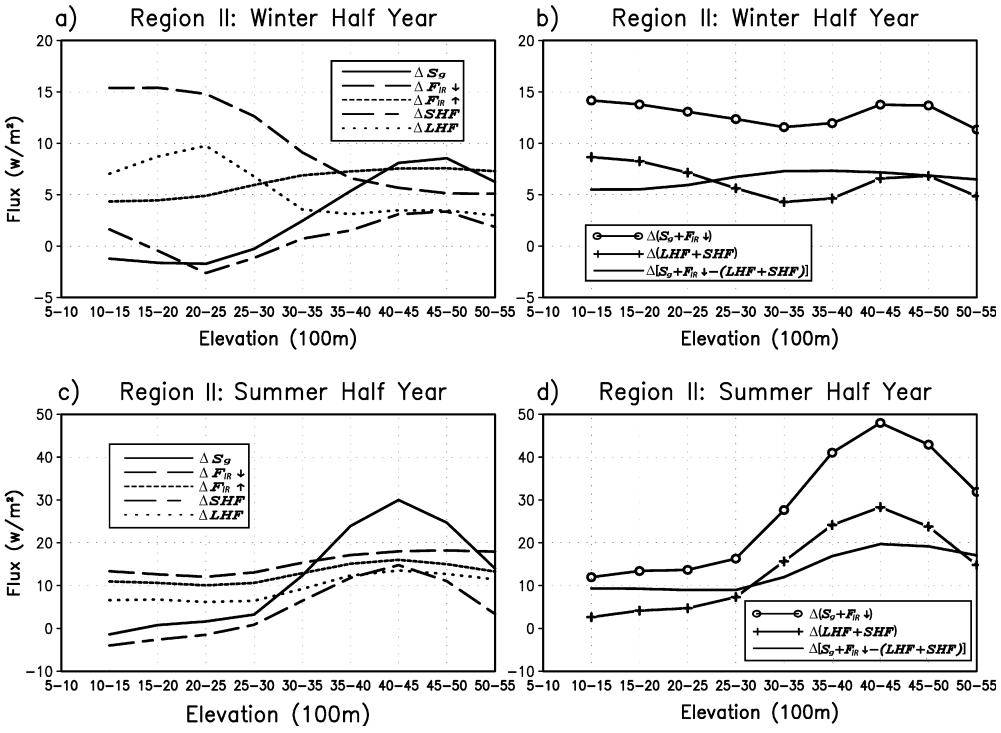

Fig. 12a–d The same as Fig. 9, but for region II

In the summer half year (Fig. 12c), the most outstanding feature in region II is that S_g significantly enhances above 3.0 km with a maximum at 4.0–4.5 km altitudes in the $2\times CO_2$ run, and this enhancement is closely associated with the snow-albedo feedback mechanism (see next section). In addition, there is a small decrease in S_g found below 3.0 km. For the $2\times CO_2$ run, $F_{IR}^{\downarrow}$ increases at all elevations and the increase also amplifies at the elevations above 3.0 km. It can be seen that the enhanced $(S_g + F_{IR}^{\downarrow})$ (Fig. 12d) is most responsible for the strong enhancement of ground temperature increase at higher elevations (see Fig. 8b). Moreover, *LHF* intensifies at all elevations with a maximum at the elevation of 4.0–4.5 km, and *SHF* shows a decline at elevations below 3.0 km and an increase above with the largest intensification at the elevation of 4.0–4.5 km. $\Delta(SHF + LHF)$ (Fig. 12d) acts to cool the surface and partially offsets the enhanced $(S_g + F_{IR}^{\downarrow})$. Finally, the net increase in $(S_g + F_{IR}^{\downarrow}) - (SHF + LHF)$ is compensated by the increase in the $F_{IR}^{\uparrow}$.

In summary, the surface energy exchange displays different characteristics for different locations and seasons, although the ground temperatures in regions I and II all show warming for both the winter and summer half years. In addition, the types of surface energy exchange responsible for the elevation dependency of ground temperature, if there is one, varies depending both on the region and on the season.

4.2.2 Factors responsible for the change in the surface energy exchange

Figure 13a, b is the same as Fig. 10a, b but for region II. In the winter half year (Fig. 13a) the cloud amount at middle and low levels increases at the elevation range of 1.0–3.0 km and decreases at elevations above 3.0 km. The largest decrease is found at 4.5–5.0 km or at 500 hPa level which is a relatively low level considering the topographic height. Related to the increased cloud amount, stronger intensification in the precipitation (not shown) is seen at lower elevations, and weaker and no intensification at higher attitudes. The role played by the increased cloud amount in the surface energy budget is very similar to that in region I. In addition, there is a peak in ΔS_g at the elevation range of 4.0–5.0 km (Fig. 12a), which is also associated with reduced snow cover there besides the largest decrease in the cloud mount. Figure 14a, b depicts the snow cover in region II for the control and $2\times CO_2$ runs as well as their difference in the winter and summer half years respectively. The snow cover in Fig. 14a, b is measured in terms of equivalent liquid water contents, which is updated in the RegCM2 through a prognostic equation involving the snow precipitation rate, the rates of sublimation and snow melt. In the winter half year (Fig. 14a) a large depletion of snow cover is found at the elevations above 3.5 km with a maximum of about 820 mm in equivalent liquid water at an elevation of 3.5–4.5 km. Due to this depletion of snow cover the surface albedo reduces, and as a result, together with decreased cloud amounts, S_g enhances as shown in Fig. 12a. In the summer half year (Fig. 13b) a mild decrease in the low-level cloud amount can be seen at the elevations of 2.0–3.5 km. Above 3.0 km the cloudiness increases with a maximum at the highest elevation. Most significantly, the snow cover dramatically reduces in an elevation range between 3.0 and 5.0 km with a largest value about 1200 mm in equivalent liquid water (Fig. 14b). The decreased surface

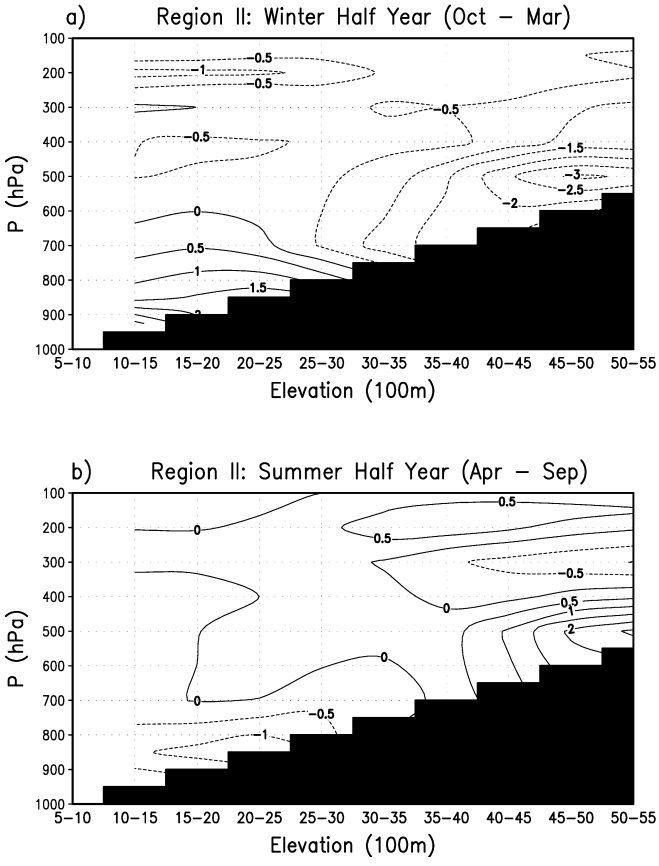

Fig. 13a, b The same as Fig. 10, but for region II

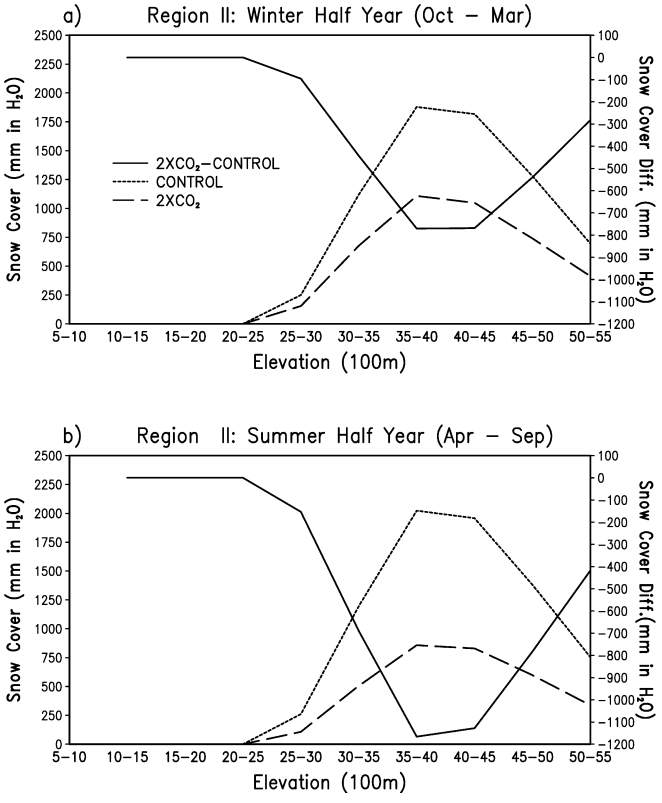

Fig. 14a, b The snow cover measured in terms of equivalent liquid water from the $2\times CO_2$ run, the control run and the difference between them as functions of elevation in region II for **a** the winter and **b** the summer half years

albedo resulting from this reduction in the snow cover leads to the strongest enhancement in S_g at the same elevations, which is a main feature in Fig. 12c. Moreover the large increase in the cloud amount shown in Fig. 13b at the highest attitudes weakens the increase in ΔS_g.

Summary and discussion

The NCAR RegCM2 with time-dependent lateral meteorological fields provided by a 130-year transient increasing CO_2 simulation of the NCAR CSM has been used to investigate the mechanism of surface warming over the TP. From our model results, when CO_2 is doubled, a strong ground warming occurs in the TP, and the two regions with the largest warming are in the eastern TP (region I) and along the southwestern and western slopes (region II). Moreover, in region I the ground warming in the winter half year is stronger than that in the summer half year, but in region II the warming difference between the seasons becomes opposite to that in region I, i.e., the warming is strong in the summer half year and weak in the winter half year. There are indications that the summer monsoon enhances but the winter monsoon weakens when CO_2 is doubled. A strong elevation dependency of ground warming is found in region I for the winter half year, and in region II for both winter and summer half years at the elevations below 5 km. The simulated characteristics of ground warming in the TP are consistent with the observations. In region I, when CO_2 is doubled, the cloud amount increases at lower elevations and decreases at higher elevation for the winter half year. In consequence, at lower elevations the short wave solar radiation absorbed at the surface declines, and the downward long wave flux reaching the surface enhances; on the other hand, at higher elevations the solar radiation flux increases and the infrared radiation flux shows a more uniform increase. The net effect of both radiation fluxes results in an enhanced surface warming at higher elevations, which is the primary cause of the elevation dependency in the surface warming. In the summer half year the clouds reduce in region I for all elevations, and there is no elevation dependency detected in the ground warming. Moreover, there is little snow existing in region I for both summer and winter half years, and the influence of snow-albedo feedback is negligible. In region II, although the changes in the cloud amount bear a resemblance to those in region I, the most significant factor affecting the surface energy budget is the depletion of the snow cover at higher elevations, which leads to a reduction of the surface albedo and, as a result, to an enhancement in the solar radiation absorbed in the surface. The snow-albedo feedback mechanism is the

most essential cause of the elevation dependency in the surface warming for region II.

Both Giorgi et al. (1997) and Fyfe et al. (1999) have shown that the snow-albedo feedback mechanism plays a major role in elevation dependency of the surface climate change signal in the Alps and Rocky mountains based on the results from two models with quite different resolutions. In particular, the model used by Fyfe et al. (1999) has a relatively coarse T32 resolution, but as they claimed, the topography of the Rockies in the model reaches high enough over a large enough area to be able to support appreciable winter and spring snow cover. In both studies, reduced snow cover in high elevation is essential to the elevation effect. Compared with the Alps and Rocky mountain complexes, the TP has much larger area and higher elevations as well as far more terrestrial regimes. In the NCAR CSM transient increasing CO_2 run (having a T42 resolution), used as the lateral forcing for the RegCM2 in our study, there is no clear elevation dependency detected over the TP (not shown), although snow depletion occurs when the CO_2 concentration reaches doubling level, suggesting other factors may play a role in the topography dependency in the TP. Our model results from the RegCM2 indicate that, besides the snow-albedo feedback, the enhanced cloud amounts and precipitation are also responsible for the elevation dependency of surface warming in the TP, particularly in the eastern TP. The topography forced cloudiness and precipitation are certainly underestimated in the NCAR CSM because of a much smoother topographical representation for the TP.

Moreover, during the summer half year, in addition to precipitation induced by low level convergence associated with the monsoon flows and upward motions dynamically forced by topography, at high elevations, surface heating also destabilizes the overlying atmosphere and enhances convective precipitation. Thus the local response to global warming over the TP is much more complicated than that in winter half year. In order to get more reliable results, an accurate simulation of summer monsoon is essential for either the GCM or the regional model.

Finally, it should be pointed out that our results here should not be viewed as a quantitative estimation of climate change or climate predication because they are only based on sensitivity of climate to atmospheric CO_2 concentration. Our purpose is only to suggest a physical interpretation for the elevation effect on climatic warming in the model, which has an observational counterpart. Many more numerical experiments need to be done in order to get results more applicable to the real atmosphere.

Acknowledgements The authors would like to thank Drs. J. Qian and X. Bi for providing the model code and data. They also wish to express appreciations to Dr. C. Liu at NCAR and Mr. C. Hung at UCLA for their help in processing the NCAR CSM outputs. The authors are grateful to two anonymous reviewers for their constructive comments. The first author thanks Prof. Zhisheng An for his hospitality and valuable discussions. The first two authors acknowledge the support from NASA/Office of Earth Science; and the first and last authors acknowledge the support from the NKBRSF (G1999043401), NSFC (40121303, 40023003) and CAS President Fund.

Appendix A

Testing the difference between means

To test statistical significance of the simulated ground temperature difference between the control and $2\times CO_2$ runs, a simple approach is used (e.g. Freund and Walpole 1987). Let $\{x_1, x_2,\ldots, x_n\}$ and $\{y_1, y_2,\ldots, y_m\}$ be two independent random samples with size n and m respectively. Compute their means and variances as $\bar{x} = \frac{1}{n}\sum_{i=1}^{n} x_i$ $\bar{y} = \frac{1}{m}\sum_{i=1}^{m} y_i$ and $\sigma_x = \frac{1}{n}\sum_{i=1}^{n} (x_i - \bar{x})^2 \sigma_y = \frac{1}{m}\sum_{i=1}^{m} (y_i - \bar{y})$. Suppose we want to test the null hypothesis: $H_0 : \bar{x} - \bar{y} = 0$ against the alternative $H_1 : \bar{x} - \bar{y} \neq 0$. The V defined by $V = \frac{\bar{x}-\bar{y}}{\sqrt{\sigma_x/n+\sigma_y/m}}$ has a than 1.96, the null hypothesis can be rejected at the 95% confidence level, in other words, the difference between $\bar{x}$ and $\bar{y}$ is significant at the 95% significance level. The means and variances of averaged ground temperature for the area in Fig. 3 are calculated with a sample size of 1095 (last three years). They are 278.9 °K (mean) and 59.9 $(°K)^2$ (variance) for the control run, and 280.9 °K and 66.9 $(°K)^2$ for the $2\times CO_2$ run. Then the $V = 5.88 >$ 1.96 is obtained. Therefore the ground temperature difference between two runs is statistically significant and conclusive at the 95% significance level.

References

Aizen VB, Aizen M, Melack JM, Dozier J (1997) Climatic and hydrologic changes in the Tien Shan, central Asia. J Clim 10: 1393–1404

Beniston M, Rebetez M (1996) Regional behavior of minimum temperatures in Switzerland for the period 1979–1993. Theor Appl Climatol 53: 231–244

Beniston M, Diaz HF, Bradley RS (1997) Climatic change at high elevation sites: an overview. Clim Change 36: 233–251

Cubash U, Hasselmann K, Hock H, Maier-Reimer E, Mikolajewicz U, Santer BD, Sausen R (1992) Time-dependent greenhouse warming computations with a coupled ocean–atmosphere model. Clim Dyn 8: 55–69

Dickinson RE, Henderson-Sellers A, Kennedy PJ (1993) Biosphere–Atmosphere Transfer Scheme (BATS) Version 1e as Coupled to the NCAR Community Climate Model. NCAR Tech Note NCAR/TN-387 + STR, 72pp

Freund JE, Walpole RE (1987) Mathematical statistics, 4th edn. Prentice-Hall, Englewood Cliffs, NJ 07632, USA, pp 412–445

Fyfe JC, Flato GM (1999) Enhanced climate change and its detection over the Rocky Mountains. J Clim12: 230–243

Giorgi F, Marinucci MR, Bates GT (1993a) Development of a second generation regional climate (RegCM2): boundary layer and radiative transfer processes. Mon Weather Rev 121: 2794–2813

Giorgi F, Marinucci MR, De Canio G, Bates GT (1993b) Development of a second generation regional climate (RegCM2): convective processes and assimilation of lateral boundary conditions. Mon Weather Rev 121: 2814–2832

Giorgi F, Hurrell J, Marinucci MR, Beniston M (1997) Elevation dependency of the surface climate change signal: a model study. J Clim 10: 288–296

Grell GA, Dudhia J, Stauffer DR (1994) A description of the fifth generation Penn State/NCAR Mesoscale Model (MM5). NCAR Tech Note NCAR/TN-398 + STR, 121pp

Holtslag AAM, de Bruijn EIE, Pan HL (1990) A high resolution air mass transformation model for short-range weather forecasting. Mon Weather Rev 118: 1561–1575

Houghton JT, Filho LGM, Callander BA, Harris N, Kattenberg A, Maskell K (eds) (1996) Climate change 1995: the science of climate change. Cambridge University Press, Cambridge, UK

Kato H, Nishizawa K, Hirakuchi H, Kadokura S, Oshima N, Giorgi F (2001) Performance of RegCM2.5/NCAR-CSM nested system for the simulation of climate change in East Asia caused by global warming. J Meteor Soc Japan 79: 99–121

Kattenberg A, Coauthors (1996) Climate models – projections of future climate, climate change 1995: the science of climate change. Cambridge University Press, Cambridge, UK, pp 285–357

Kiehl JT, Briegleb BP (1991) A new parametrization of the absorptance due to the 15 μm band system of carbon dioxide. J Geophys Res 96: 9013–9019

Kutzbach JE, Prell WL, Ruddiman WF (1993) Sensitivity of Eurasian climate to surface uplift of the Tibetan Plateau. J Geol 101: 177–190

Liu XD, Chen BD (2000) Climatic warming in the Tibetan Plateau during recent decades. Int J Climatol 20: 1729–1742

Manabe S, Terpstra TB (1974) The Effects of mountains on the general circulation of the atmosphere as identified by numerical experiments. J Atmos Sci 31: 3–42

Manabe S, Broccoli AJ (1990) Mountains and arid climate of middle latitudes. Science 247: 192–195

Manabe S, Stouffer RJ, Spelman MJ, Bryan K (1991) Transient response of a coupled ocean–atmosphere model to gradual changes of atmospheric CO_2. Part I: annual mean response. J Clim 4: 785–818

Meehl GA, Washington WM, Arblaster JM, Bettge TW, Strand WG (2000) Anthropogenic forcing and decadal climate variability in sensitivity experiments of twentieth- and twenty-first-century climate. J Clim 13: 3278–3744

Murphy JM, Mitchell JFB (1995) Transient response of the Hadley Centre coupled ocean–atmosphere model to increasing carbon dioxide, Part II: spatial and temporal structure of the response. J Clim 8: 57–80

Tang MC, Cheng GD, Lin ZY (Eds) (1998) Contemporary climatic variations over the Qinghai-Xizang (Tibet) Plateau and their influences on environments. Guangdong Science and Technology Press, 229pp (in Chinese)

Thompson LG, Mosley-Thompson E, Davis ME, Lin N, Yao T, Dyurgerov TM, Dai J (1993) ''Recent warming'': Ice core evidence from tropical ice cores, with emphasis on central Asia. Global Planet Change 7: 145–156

Webster PJ, Yang S (1992) Monsoon and ENSO: Selectively interactive system. Q J R Meteorol Soc 118: 877–926

Yao T, Lonnie G, Thompson LG, Yang Z (1995) Recent warming as recorded in the Qinghai-Tibet cryosphere. Ann Glaciol 21: 196–200

Yanai M, Li C, Song Z (1992) Seasonal heating of the Tibetan Plateau and its effects on the evolution of the summer monsoon. J Meteorol Soc Japan 70: 319–351

Yeh T-C, Gao Y-X (1979) The Meteorology of the Qinghai-Xizang (Tibet) Plateau. Science Press: Beijing, 278pp (in Chinese)